

Behaviour of sub-clad and through-clad cracks under consideration of the residual stress field

Jörg Hohe*, Marcus Brand, Dieter Siegele

Fraunhofer Institut für Werkstoffmechanik
Wöhlerstr. 11, 79108 Freiburg, Germany

March 5, 2009

Abstract

Aim of the present study is an assessment of the behaviour of cracks in the ferritic base metal of components supplied with an austenitic welded cladding under special consideration of the residual stress field caused by the welding and heat treatment processes. For this purpose, an experimental and numerical investigation has been performed. The experimental study consisted of two component tests at low temperature using large-scale specimens with sub-clad and surface cracks. Subsequently, the experiments were analyzed numerically where the residual stress field was determined in an advanced numerical simulation of the welding and heat treatment processes. Based on the results, a fracture mechanics assessment of the ferritic and austenitic material zones on crack initiation and arrest was performed. The experimental and numerical results reveal that fracture was initiated in the ferritic range whereas the austenitic cladding remained intact even in the case of a limited crack extension in the base metal underneath the cladding.

Key words: Cladding, Fracture behaviour, Welding process, Residual stresses, Component tests.

1 Introduction

In electric power generation technology as well as in many other technological fields, clad ferritic pressure vessels and pipes are used, where the load carrying ferritic base metal is protected against corrosion by an austenitic welded cladding. The structural integrity assessment of this type of components is a complex task, since the welding and heat treatment processes and the mismatch in the thermo-mechanical properties of the two bonded materials in general result in complex residual and thermally induced stress fields. Furthermore, the non destructive testing of clad components might be more complicated compared to non-clad ones, especially with respect to the detection of sub-clad cracks in the ferritic base metal underneath the cladding. On the other hand, due to the ductile material response of the austenitic cladding material even at deep temperatures, the cladding may have advantages with respect to the fracture characteristics since it partially shields the crack and thus reduced the risk of brittle failure of the ferritic range.

In the industrial design process, the fracture assessment of clad components is usually performed by means of a two-step procedure consisting of a stress analysis of the uncracked component under consideration of the cladding and a subsequent fracture assessment using analytical formulae. In this procedure, the cladding is either assumed to be cracked or neglected (e.g. ASME Code [2], German KTA rules [3]). As an alternative, specialized analytical formulae for post-analysis fracture assessment of cracks under consideration of the cladding have been proposed by Blauel et al. [6], Hodulak and Siegele [9], as well as in a recent study by Marie and Chapuliot [12]. A more physical but still approximate approach based on plastic corrections of an elastic structural analysis has been provided by Marie and Nédélec [13]. Nevertheless, all of the mentioned approaches provide approximations of the stress and displacement fields and in general do not account for the local residual stress state caused by the manufacturing process. Furthermore, they rely on the assumption that the cladding remains intact.

Aim of the present study is the experimental and numerical investigation of the behavior of cracks in ferritic components supplied with an austenitic cladding considering both, sub-clad and through-clad surface cracks.

*Corresponding author. Tel: +49-761-5142-340, Fax: +49-761-5142-401, E-mail: joerg.hohe@iw.fraunhofer.de

For this purpose, two large-scale specimens consisting of a ferritic pressure vessel steel were clad with an austenitic material and supplied with a surface and a sub-clad crack respectively. The specimens were tested under thermo-mechanical loading conditions. Both specimens failed in a brittle mode initiated in the ferritic material. For the specimen with through-clad crack, a first initiation was followed by a crack arrest before final fracture occurred at a significantly higher load level. For the specimen with sub-clad crack, no interim crack extension and arrest prior to final fracture was observed. In both cases, the cladding remained intact until the ultimate fracture of the specimens.

Subsequently, the local conditions triggering crack initiation and arrest were analyzed numerically under consideration of the residual stress fields caused by the manufacturing process which were determined by means of a detailed analysis of the welding and post weld heat treatment processes. The residual stress field was found to have a complex periodic character with distinct local variations. In the subsequent analysis of the fracture experiments, it was demonstrated that the brittle failure of the base metal was the more critical fracture event compared to a possible ductile crack extension into the cladding. An excellent agreement was obtained between the experimental and numerical results.

2 Material and properties

2.1 Material

The base material used in the experimental investigation was a German 22 NiMoCr 3-7 nuclear grade pressure vessel steel (similar to A 508, class 2). The material was taken from the cylindrical shell of a reactor pressure vessel originally intended for a power plant that finally has not been constructed. The material was forged followed by a heat treatment consisting of an austenization at $T = 900^\circ\text{C}$. Subsequently, the shell was quenched in water, tempered at $T = 650^\circ\text{C}$ for 7.5 h followed by cooling in air. More details on the material, especially the chemical composition, can be found in a previous study on a different topic (Hohe et al. [11]), where the same heat of the material was employed, nevertheless in a different state of heat treatment.

From the center section of the shell, two large plates with dimensions of $700 \times 300 \times 74$ mm and three small plates with the dimensions $360 \times 155 \times 55$ mm were cut. The large plates were used as large-scale fracture specimens whereas the small-scale specimens for the basic characterization of the material were extracted from the small plates. All five plates were supplied with a double layer austenitic cladding consisting of CN 24/13 NBR 800 BS for the first layer whereas CrNi 21/10-BS electrodes were used for the second layer. The main difference of the materials was a slightly higher content of chromium in the material of the first layer. Both layers were welded with strip electrodes with a width of 60 mm in a sub-merged arc welding process with an electrical current of 700 A and a voltage of 28.5 V. The welding was performed with an overlap of the individual welds of 15 mm. The individual layers were approximately 4 mm thick. After the cladding process, the plates were subjected to a post weld heat treatment at $T = 600^\circ\text{C}$ for duration of ten hours with a heating and subsequent cooling period of about 50 h. Both, the cladding and the heat treatment processes were performed in accordance with the relevant German nuclear standard KTA 3201 [3].

For an investigation of the microstructure of the material and the identification of the different material ranges, a section has been prepared from one of the small plates. The section was orientated normal to the welding direction. The results of the metallographic investigation are presented in Fig. 1. The two individual cladding layers have a thickness of 4 mm to 5.5 mm, depending on the position within the plate. Below the ferritic and austenitic interface, a heat affected zone with a depth varying periodically with the position underneath the individual welding seams of the first cladding layer is detected. The average depth of the heat affected zone is approximately 10 mm. Within the heat affected zone, a much coarser grain size compared to the base metal has developed. Directly at the interface, the microstructure might also be affected by diffusion processes during the welding process, affecting the local C-content.

2.2 Thermo-physical and mechanical characterization

In the numerical simulations, the static mechanical material response was described in terms of standard isotropic elasto-plasticity using Hooke's law and Mises J_2 -plasticity with polylinear hardening. The respective material parameters were determined from tensile tests of round bars with a diameter of 2 mm and 20 mm gauge length. The characterization was performed separately for each of the different material zones (base metal, heat affected zone, first and second layer of the cladding). The specimens from the austenitic material ranges were extracted from the center of the respective cladding layer whereas the specimens from the ferritic ranges were extracted

in depths of 2 mm and approximately 17.5 mm below the ferritic/austenitic interface for the heat affected zone and the base metal, respectively. All tensile specimens were orientated longitudinal to the welding direction. The tests were performed throughout the relevant temperature ranges for the component tests and the simulation of the welding process ranging from $T = -150^{\circ}\text{C}$ up to $T = 1000^{\circ}\text{C}$. In Fig. 2, the measured true stress vs. true strain curves for the four different material zones are presented. In this context, the true (logarithmic) strain has been determined from optical diameter measurements during the tests. Since the optical diameter measurement failed at temperatures of $T = 800^{\circ}\text{C}$ and beyond due to heavy oxidation of the specimen surfaces, no logarithmic stress strain curves are available for some cases. In these cases, ideally plastic material behaviour with the initial yield stress as a constant yield stress was assumed in the numerical analyses whereas in all other cases, the obtained yield curves were employed for characterisation of the elastic-plastic material response.

For the simulation of the heat treatment process, the creep response of the material in the relevant temperature range for the post weld heat treatment was determined. For this purpose, relaxation experiments on round tensile specimens with 2.8 mm diameter and approximately 35 mm gauge length were performed at temperatures of $T = 450^{\circ}\text{C}$, 525°C and 600°C respectively. The specimens were extracted from the small plates at similar positions as the R(T) 2x20 specimens for the static tests. From the relaxation characteristics, the parameters of Norton's creep law were determined.

For the simulation of the welding process, a further characterization of the material with regard to the thermo-physical properties was necessary. The density and the coefficient of thermal expansion were determined in dilatometric experiments whereas the specific heat capacity and the thermal conductivity were determined in dynamic calorimetric experiments and by a laser flash analysis, respectively. In all cases, small-scale cylindrical specimens have been used which were extracted in a similar manner from the small plates as the round tensile bars for the mechanical characterization. The thermo-physical properties were determined throughout the relevant temperature range for the welding process (ambient temperature up to $T = 1200^{\circ}\text{C}$ to 1400°C).

The fracture toughness of the base metal was characterized by fracture tests of SE(B) 10x10 specimens with a crack depth ratio of $a/W = 0.5$. For a realistic determination of the fracture toughness of cracks in the ferritic material directly underneath the cladding, two of the small plates were supplied with a 10 mm deep surface crack prior to the cladding process. After the cladding and heat treatment processes, the specimens were machined carefully from the pre-cracked plates such that the desired crack depth was achieved. In order to keep heat effects due to the manufacturing process as low as possible, electrical discharge machining was used for the specimen manufacturing process. The SE(B) 10x10 specimens were tested according to ASTM standard E 1921 [1] in the temperature range between $T = -70^{\circ}\text{C}$ and -90°C . Due to the extraction of the plates from the center of the original pressure vessel shell and the additional heat treatment, a tougher behaviour of the material with $T_0 = -95.6^{\circ}\text{C}$ compared to earlier investigations on the same heat (Hohe et al. [11]) was obtained.

The ductile fracture characteristics of the cladding were characterized in terms of J_R crack resistance curves. Since – due to the limited thickness of the cladding layers – no valid crack resistance curves could be determined by direct measurements, estimated crack resistance curves were determined by a simulation of a virtual experiment of a C(T) 25 specimen using the material data for the individual cladding layers as determined before. The crack extension process was modelled by using Gurson's [7] ductile damage model with parameters which were determined by a finite element simulation of the tensile tests of the cladding material. Full details on the experimental procedures and the complete set of results can be found in the final report on the respective research project (Hohe et al. [10]).

3 Large-scale fracture experiments

3.1 Experimental set-up

For an experimental investigation of the behaviour of sub-clad and through-clad cracks in cladded components, two fracture tests using the two large plates (see Section 2.1) were performed. One of the plates was supplied with a sub-clad crack by providing it with a semi-elliptical started notch with a length of 40 mm and a depth of 8 mm prior to cladding. The notch was fatigued under three-point bending with a final load level of approximately $K_I = 20 \text{ MPa}\sqrt{\text{m}}$. Subsequently, the crack was cladded over. The second plate was supplied with a through-clad surface crack by a similar procedure after the cladding and heat treatment. The starter notch was of similar shape and dimensions within the base metal as for the specimen with sub-clad crack whereas it had straight vertical edges within the cladding. Both cracks were located symmetrically in the center of the specimens on the cladded side. The external geometry of the large-scale specimens together with the crack location and the coordinate system employed in all subsequent diagrams is presented in Fig. 3.

Prior to testing the specimens under thermo-mechanical loading conditions, the non-cladded areas on the longitudinal sides of the specimens were removed in order to avoid non properly defined conditions in the tests due to the different width and non-straight edges of the cladding on both sides as well as the varying cladding thickness during the transition from cladded to non cladded areas. For this purpose, 40 mm of the specimen width was removed from each side, reducing the total specimen width to 220 mm. For the same reason and in order to provide smooth supports for the rollers of the mechanical loading device, the cladding ends were partially removed (see Fig. 3).

The specimens were tested under combined thermo-mechanical loading conditions. In this context, the cracked surface of the plates was cooled whereas the opposite side was kept at higher temperatures in order to ensure a brittle crack initiation at deep temperatures and, if possible, a crack arrest at less deep temperatures after a limited crack propagation into the depth of the specimen. Similar as in a previous study (Hodulak et al. [8]), the cooling was performed by application of an insulated cooling basin to the cracked surfaces of the specimens, which was filled with liquid nitrogen. The specimen surface within the cooling basin was finished with copper chips in order to enhance the heat transfer on this surface and thus to reduce the cooling times (see Fig. 3). The opposite surface was kept at higher temperatures by an electrical resistance heating. The heating power was controlled such that steady state conditions with a thermal stationary gradient ranging from close to $T = -196^{\circ}\text{C}$ on the cracked surface to ambient temperature at the opposite surface were achieved. Once steady-state thermal conditions were achieved, the specimens were loaded mechanically under displacement controlled three point bending conditions to fracture. Hence, the thermo-mechanical conditions were similar as under an assumed pressurized thermal shock scenario.

During the experiments, the resulting applied force and the cross-head displacement were recorded. In addition to the cross-head displacement, the bending deformation of the specimens was measured directly as the difference Δv_{11} of two points located on the specimen sides underneath the rollers at the end of the specimen and a point located on the specimen side in the crack plane. The temperature field was controlled by seven thermocouples applied on each side of the specimen the in the crack plane at different depths, five thermocouples in the crack plane on the cooled surface and additional thermocouples on the sides of the specimens near the electrical resistance heating. In order to detect a possible failure of the cladding, additional clip gauge measurements of the displacement difference between two points located on each side of the crack were made on the cooled surface of the specimen with sub-clad crack (see Fig. 3).

3.2 Results

The temperature distribution measured under steady state conditions on the side of both specimens during the mechanical loading phase of both experiments is presented in the first plot in Fig. 4. At the interface of the ferritic and austenitic material ranges, a temperature in the range of $T = -130^{\circ}\text{C}$ to -120°C was achieved whereas the crack front temperature at the deepest point of the fatigue pre-crack in both cases with approximately $T = -100^{\circ}\text{C}$ was slightly lower than the master curve reference temperature $T_0 = -95.6^{\circ}\text{C}$ determined before on small-scale specimens (see Section 2.2). Notice that due to different heat transfer properties of the cooled specimen surface, the temperature distributions in both experiments were slightly different.

In the second plot in Fig. 4, the measured load displacement characteristics of both tests are presented in terms of the overall resulting force F and the bending deformation Δv_{11} measured on the specimen sides. For the specimen with through-clad surface crack, a distinct drop in the resulting load by $\Delta F = 24\text{ kN}$ is observed at a displacement of $\Delta v_{11} = 1.553\text{ mm}$. The drop in the resulting load was caused by a crack extension in the ferritic material range followed by a crack arrest. During this crack extension, the cladding over the advancing crack remained intact. At $\Delta v_{11} = 2.502\text{ mm}$, final fracture of the specimen occurred.

For the specimen with sub-clad crack, no distinct interim crack extension was observed prior to final fracture of the specimen at a bending deformation of $\Delta v_{11} = 3.808\text{ mm}$ and a resulting force of $F = 1.139\text{ MN}$ (see Fig. 4). Again, the cladding remained stable and intact throughout the mechanical loading phase of the experiment. This visual observation is confirmed by the clip-gauge measurements of the relative displacement of two points located on the cracked surface on opposite sides of the crack in comparison to a similar measurement on two points near the side of the specimen outside the influence zone of the crack.

After the experiments, a fractographic investigation of the fracture surfaces of both specimens was performed using optical and scanning electron microscopy. The total fracture surfaces of both specimens and enlarged figures of the areas where the failure initiation spots were detected are shown in Fig. 5. Notice that the enlarged micrographs obtained in the SEM investigation were taken from the opposite crack surface as the optical micrographs of the total crack area.

For the specimen with sub-clad crack (top pictures in Fig. 5), no arrest crack front is visible, as expected from the overall load-displacement diagram presented in Fig. 4. The primary crack initiation spot was detected at a large sulphide inclusion close to the fatigue crack front approximately 2 mm below the ferritic and austenitic interface. The inclusion was found to be surrounded by an area of intergranular crack propagation (chain-dotted line in the scanning electron micrograph). In the ferritic material range outside this area, the failure mechanism was pure transgranular (quasi-) cleavage. Both layers of the cladding were found to have failed in a mixed mechanism with some amount of ductile voids and some amounts of cleavage failure. The occurrence of cleavage in an austenitic stainless steel as observed here is caused by a limited formation of δ -ferrite directly from the melt. The formation of δ -ferrite is caused by the alloying of the weld material with chromium in order to reduce the hot shortness. Due to the lower chromium content of the second layer, only a lower amount of cleavage failure was observed in this range. In the interphase between the two layers of the cladding, ductile failure was observed as the exclusive failure mechanism. Despite this limited tendency towards cleavage failure, no indicators for a larger failure event in the cladding prior to the final fracture of the entire specimen were observed on the fracture surface.

For the specimen with through-clad (surface) crack (bottom pictures in Fig. 5), both the initial fatigue crack and the arrest crack are clearly visible. Both, the fatigue pre-crack and the arrest crack are asymmetric due to the differences in the stress fields on both sides of the respective crack caused by the periodic residual stress field. No such asymmetry was present for the specimen with sub-clad crack, since in this case, the crack had been prepared prior to the cladding process whereas for the specimen with through-clad crack, the fatigue pre-crack was prepared after the cladding process when the residual stress field was already present. For the initial through-clad crack, the primary initiation spot for the failure of the ferritic material range was detected to be a welding crack in the cladding layer located directly above the ferritic and austenitic interface. From here the crack extended over the interface into the coarse grain zone directly underneath the interface. Although the (first) crack initiation was triggered by a defect located within the cladding, no indicators were found for a larger crack extension into the austenitic range at this instant, except possible local pop-in events. The fact that the cladding remained intact during the interim crack extension explains the relatively small drop in the resulting load of about 4.5% of the actual load level although the crack surface in the ferritic range increased approximately five times.

4 Numerical simulation

4.1 General concept

For a further assessment of the experimental results, the tests of the cladded large-scale fracture specimens were simulated numerically by means of the finite element method. The computations were performed under consideration of the residual stress field due to the welding and heat treatment processes. Therefore, not only the fracture experiments but also the manufacturing process had to be simulated. Since the requirements for the models for simulation of the welding process and for simulation of the fracture experiments regarding the mesh resolution, the area to be modelled as well as the analysis technique are quite different, a multi-step analysis procedure has been developed. This procedure consists of a sequence of multiple analyses for the different manufacturing and loading steps according to Fig. 6. For each step, different appropriate discretizations and analysis codes were utilized. The solution at the end of each step was transferred as initial condition to the model for analysis of the following step.

The analysis of the welding process had to be performed with a model of the full plates due to the asymmetry of the thermal loading conditions during the welding of the individual welding seams. Due to the high temperature and strain gradients in the vicinity of the actual position of the heat source, a high mesh resolution was required throughout the cladding and the adjacent areas of the base metal. The analysis was performed as a sequentially coupled thermo-mechanical analysis where the temperature field was computed in a first step and subsequently applied as a load for the mechanical analysis. For reasons of simplicity, the analysis of the post weld heat treatment was performed with the same finite element model as the welding process. Due to the low heat and cooling rates, no transient heat transfer problem was solved but the time dependent temperature field was applied directly as a prescribed thermal load to the finite element model. In both analysis steps, the crack was not considered.

Subsequently, the fracture experiments on the cladded plates were simulated. As usual in fracture mechanics, finite element meshes were used which were focussed to the crack front, whereas coarse discretizations were sufficient far from the respective crack front. Due to the symmetry of the loading conditions, only the rear half of the specimens was modelled since the residual stress field after the post weld heat treatment proved to be sufficiently symmetric with respect to the crack plane. Nevertheless, the second geometric symmetry of the

specimens with respect to the longitudinal axis could not be exploited due to the distinct asymmetry of the residual stress field with respect to this direction. In the case of the specimen with through-clad crack, two different models were used to simulate the state prior to and after the intermediate crack initiation and subsequent arrest. Again, the simulation was performed as a sequentially coupled thermo-mechanical analysis, where the temperature field was computed in a first step and subsequently applied as a prescribed thermal load to the second step, where the mechanical problem was solved.

Within this multi-step analysis procedure, the thermal and the mechanical simulations of the welding process were performed by the welding analysis code SYSWELD [5]. For the simulation of all subsequent steps including the simulation of the post weld heat treatment as well as the thermal and mechanical simulations of the fracture experiments, the multi-purpose finite element program ABAQUS [4] was employed.

4.2 Welding and post weld heat treatment processes

The simulation of the welding and post weld heat treatment processes was performed by means of a finite element model of the full specimen geometry. The geometry was discretized by 147315 displacement or temperature based tri-linear 8-node elements with reduced integration. The elements forming the cladding seams were initially deactivated and became active, once the welding heat source passed the respective position. In the thermal analysis, the heat input by the strip electrode arc welding process was modelled by means of a simplified semi-cylindrical heat source moving at the respective welding speed along the individual seams. The heating power of the simplified heat source was adapted such that the transient temperatures determined with thermocouples at different locations beside the cladded area during the cladding process was recovered. The transient temperature field during the welding of the two times five individual seams forming the two cladding layers was recorded and applied as a prescribed thermal condition for the subsequent mechanical analysis of the welding process, where the development of the elastic and plastic deformation due to the thermal loading conditions under consideration of phase changes and thus the resulting residual stress field were determined.

The residual stress field after welding of the final seam and complete cooling down to ambient temperature was recorded and applied as an initial condition to the finite element model for the analysis of the post heat treatment. In this analysis, an identical finite element discretization of the plates was employed. Nevertheless, due to the low temperature rates during the heating and cooling periods, no transient heat transfer analysis was performed. Instead, a uniform distribution of the transient temperature was assumed and applied directly onto the model for the mechanical analysis of the heat treatment process. In contrast to the simulation of the welding process, where a rate independent ideal plasticity model was used, Norton's creep law was employed in the analysis of the heat treatment in order to compute the stress relaxation at elevated temperatures. More details of the analyses of the welding and heat treatment processes can be found in a previous publication (Siegele and Brand [14]).

The resulting residual stress field directly after the cladding process and after the heat treatment process is presented in Fig. 7, where the first row of subfigures refers to the situation prior to the heat treatment whereas the second row is directed to the final residual stress field after the heat treatment. The stress component σ_{11} presented in the first line of subfigures is the stress component perpendicular to the welding direction whereas the component σ_{22} presented in the bottom two subfigures is the residual stress component within the welding direction. In all cases, the residual stresses are extracted within the crack plane along straight paths parallel to the specimen surface. The stress components for the two cladding layers were taken in the center of the respective layer, the residual stresses for the heat affected zone of the base metal were extracted 2 mm below the ferritic and austenitic interface whereas the residual stress results termed "base metal" refer to positions 12 mm below the interface.

As a result of the cladding process, a residual stress field with a periodic character and distinct stress peaks is obtained. Extreme values in the range of the last welding seam on the left hand side of the plots presented in Fig. 7 are caused by the fact that no stress reduction due to the welding of subsequent seams occurs in this range. In the center of the plate, stress peaks ranging from approximately 300 MPa in the tensile range to -300 MPa in the compressive range are observed. The distinct oscillations of the residual stress field are significantly reduced by a stress relaxation during the post weld heat treatment. Nevertheless, the residual stress field retains its periodic character. Since the stress relaxation occurs at an elevated temperature of $T = 600^\circ\text{C}$, residual stresses re-develop due to the mismatch in the coefficient of thermal expansion of the ferritic and austenitic ranges when the specimen is cooled down to ambient temperature. Due to this effect, the residual stress field in the base metal changes its sign and becomes compressive instead of being tensile as directly after the cladding process. The thermal mismatch also results in a slight increase of the tensile residual stresses in the cladding. Hence, the

residual stress field in clad components due to the welding and heat treatment processes is a complex field caused by the manufacturing process itself as well as by the thermo-mechanical mismatch of the two materials and cannot easily be predicted without a proper consideration of all different effects.

4.3 Fracture tests

Subsequently to the analysis of the manufacturing process, the fracture mechanics tests on the two large-scale specimens were simulated using the residual stress field computed before as an initial condition. In this case, the rear halves of the specimens were discretised by 20-node volume elements with quadratic interpolation of the displacement and temperature fields. Along the crack fronts, focussed discretizations were used, whereas coarser discretizations were judged to be sufficient far from the crack fronts. The crack front geometries were taken from the measurements made during the fractographic investigation. The employed finite element models are presented in Fig. 8. Since neither the residual stress field (see Fig. 7) nor the crack geometries were sufficiently symmetric with respect to the center plane parallel to the x_2 - x_3 -plane (see Fig. 5), the symmetry of the external specimen geometry with respect to this plane could not have been exploited. The interim crack extension and arrest observed in the test of the specimen with through-clad (surface) crack was included by using two different finite element models with the crack geometry prior to and after the crack extension and arrest between which the results were transferred at the instant of the interim crack initiation and arrest.

The analysis again was performed as a sequentially coupled thermo-mechanical analysis, where the temperature field was computed in a first step without any consideration of the deformation. Subsequently, the temperature field was applied as a prescribed thermal load to the mechanical analysis. Due to the short mechanical loading period, steady-state heat transfer conditions were assumed in the thermal analysis. The thermal model was loaded by convection boundary conditions on all external surfaces. The heat transfer coefficients for the free surfaces were set to small values resulting in a nearly thermally insulated behaviour whereas the heat transfer coefficients in the area of the cooling basin as well as in the area of the electrical resistance heating were adapted such that the computed temperature distributions along the specimen sides coincided with the measured temperature distribution (see Fig. 4). The material behaviour in the thermal analysis model was assumed to be governed by the standard linear heat transfer equation where the thermal conductivities for the individual material ranges (both cladding layers, heat affected zone and base metal) were taken directly from the temperature dependent measurements during the basic characterization of the material in Section 2.2.

The subsequent mechanical analysis was performed within the geometrically linear framework using the steady-state temperature field as a prescribed thermal load and the residual stress field computed before as an initial condition. In this context, the preparation of the specimens to their final size by removal of parts of the specimen sides (see Fig. 3) and its effect on the residual stress field was also included in the analysis, since the residual stress field was transferred from the 300 mm wide model used in the simulation of the manufacturing process to the 220 mm wide models for the analysis of the fracture experiments. Hence, a preliminary analysis had to be performed between the application of the initial conditions and the application of the steady-state temperature field in order to re-gain equilibrium and thus to obtain the altered residual stress field after machining the specimens to their final width. The models were loaded by a prescribed displacement of rigid cylinder representing the central roller of the three-point bending device which was modelled to interact with the specimen via a unilateral contact formulation. The material response was prescribed by standard J_2 -elasto-plasticity with isotropic hardening using the respective temperature dependent elastic constants and yield curves according to Fig. 2 as well as the coefficients of thermal expansion as determined in the basic characterization of the four different material ranges.

From the finite element results, the local J -Integral along the crack front as well as the corresponding local temperature T was extracted at the instants of the interim initiation and arrest for the specimen with through-clad crack as well as at the instants of final fracture for both specimens. In this context, the local position along the crack front was expressed in terms of a local coordinate s measured along the crack front with its origin on the crack front in the specimen center (see Fig. 8). The (ductile) integrity assessment of the cladding was performed directly in terms of the local J -Integral whereas the local stress intensity factor $K_J = (JE/(1 - \nu^2))^{1/2}$ according to ASTM E 1921 [1] as computed from the local J -Integral in conjunction with the elastic constants E and ν for the corresponding local temperature $T(s)$ was employed for an assessment of the brittle failure of the ferritic material ranges. The formal conversion of the local elasto-plastic J -Integral into the (local) stress intensity factor K_J as a measure for the crack driving force in the brittle ferritic ranges allows the direct comparison with the fracture probability curves for the brittle material ranges determined in Section 2.2 according to the procedure described in ASTM standard E 1921 [1]. Nevertheless, although formally a stress intensity factor K_J is deter-

mined, the it should be noticed that the fracture assessment is in fact performed in terms of the J -Integral. The results are presented in Fig. 9.

In the first subfigure of Fig. 9, the local stress intensity factors $K_J(s)$ along the crack front within the ferritic material range are presented as a function of the corresponding local temperatures $T(s)$ for the different instants considered. In addition, the fracture toughness curves for 5%, 50% and 95% failure probability according to the master curve concept (ASTM E 1921 [1]) are plotted, using the reference temperature $T_0 = -95.6^\circ\text{C}$ as measured for a depth of 10 mm below the ferritic and austenitic interface during the basic characterization of the material (Section 2.2). For the specimen with sub-clad crack at the instant of final fracture, a moderately high local load level K_J in the range between approximately $65 \text{ MPam}^{1/2}$ and $80 \text{ MPam}^{1/2}$ is obtained. Due to the asymmetric residual stress field, slight differences are obtained between the right and left hand sides of the crack front, although the crack geometry in this case was close to the symmetric case. The highest local load levels are obtained at the transition between the heat affected zone and the pure base metal. Nevertheless, the point of the highest local failure probability $P_f(s)$ is found at a location much closer to the interface of the ferritic and austenitic material ranges. This position coincides almost perfectly with the primary crack initiation spot located approximately 2 mm below the interface as detected in the fractographic investigation (see Fig. 5). Due to the presence of a rather large sulphide inclusion close to the crack front in this range, cleavage was initiated at a nominal failure probability of $P_f = 20.6\%$ distinctively below the 50% failure probability curve.

For the specimen with through-clad crack, more distinct differences between the local conditions on both sides of the crack are obtained due to the stronger asymmetry of the crack geometry. At the instant of the (first) initiation of the initial fatigue pre-crack, a local load distribution $K_J(T)$ is obtained, which attains its maximum directly at the interface of the ferritic and austenitic material ranges, whereas only rather small values well below the 5% failure probability curve are obtained at the deepest point of the crack. Again, the location of the maximum local failure probability $P_f(s)$ coincides with the location, where the primary crack initiation was detected in the fractographic analysis. In this case, a nominal local failure probability of approximately 50% was reached. At the instant of crack arrest after the crack extension following the initiation of the original fatigue pre-crack, much lower local crack front loads $K_J(T)$ are obtained. As it could be expected, the local variations of the crack front load are also much less distinct, ranging from approximately $20 \text{ MPam}^{1/2}$ to $40 \text{ MPam}^{1/2}$. The subsequent further increase of the external load F causes the local crack front loads to increase again. At the instant of final fracture, the maximum local load level $K_J(s)$ reaches approximately the same load level as at the instant of the initiation of the original fatigue pre-crack. Again, the largest local failure probability with $P_f(s) \approx 50\%$ is obtained directly at the interface of the ferritic and austenitic material ranges. Thus, a initiation in this region is most likely.

In the second subfigure in Fig. 9, the local J -Integral is plotted as a function of the local coordinate s at the different instants considered. For an assessment of the risk of a ductile crack initiation, the load levels J are marked, where ductile crack extensions of $\Delta a = 0.1 \text{ mm}$, 0.2 mm and 0.3 mm have to be expected for the material of the first cladding layer according to the approximated J_R crack resistance curve as determined during the basic characterization of the material (Section 2.2). For the specimen with sub-clad crack, the maximum value of the local J -Integral with $J = 75.5 \text{ N/mm}$ is obtained at the center of the crack front of the cladding side of the crack. This value is far below any definition of ductile initiation toughness and thus agrees well with the experimental observation that the cladding remained intact until the final fracture of the specimen.

For the specimen with through-clad crack, the maximum J -Integral at the instant of the brittle initiation of the fatigue pre-crack into the ferritic material range is obtained at the interface of the two individual cladding layers. With $J_{\max} = 84.2 \text{ N/mm}$, a similar maximum value as for the sub-clad crack is obtained, indicating a vanishing risk of material failure for the cladding. After the crack propagation underneath the cladding, much larger values of the local J -Integral are obtained. Distinct peaks of the local crack front load are observed at the corners where the original fatigue crack front intersects with the interface between the ferritic and austenitic material ranges. At this point, the interaction between the stress concentrations caused by the crack front and by the sharp kink of the crack front interact, resulting in the observed distinct local peak in the J -Integral $J(s)$. Nevertheless, the range of the crack front, where the technical initiation value $J_{0.2} = J(\Delta a = 0.2 \text{ mm})$ is exceeded, is limited to a rather short portion of the crack length. In these ranges, a limited ductile crack extension Δa has to be expected. On the other hand, a limited ductile crack extension – which was not considered in the numerical analysis – would result in a blunting of the sharp corner assumed in the idealized finite element model followed by a decrease of the local crack front load. Hence, except some limited local ductile crack extension in an area, where the finite element model was over-simplified, no large-scale failure of the cladding prior to the final failure of the specimen initiated in the ferritic material range is predicted, coinciding with the experimental observations.

5 Conclusions

The objective of the present study was an investigation of the effect of the cladding and the related residual stress field of the fracture behavior of cracks within the base metal of ferritic components supplied with an austenitic welded cladding. The investigation consisted in a combined experimental and numerical approach where two large-scale component-like clad specimens with sub-clad and through-clad cracks were tested. Subsequently, the experiments were simulated numerically in order to determine the local conditions along the crack front during the different failure events.

The residual stress field was determined in a numerical high resolution analysis of the welding and heat treatment processes. The residual stress field has a complex periodic character. It is caused by both, the welding process and the mismatch in the coefficients of thermal expansion of the bonded materials. Its determination by a numerical simulation requires great care with respect to the modelling especially of the heat input.

In the experimental fracture mechanics investigation, it was observed that under the applied low temperature conditions both, the specimen with sub-clad crack and the specimen with surface crack failed in a brittle mode initiated in the ferritic range underneath the cladding. The cladding remained intact and stable even during a distinct local crack extension in the ferritic range underneath the cladding. The numerical results obtained in the subsequent finite element simulation of the experiments were found in an excellent agreement with the experimental observations. It was proved that the brittle failure of the ferritic base metal is the more critical fracture event compared to a possible ductile crack extension into the austenitic clad material. Despite the fact that – as every weldment – the presence of the cladding might enhance the risk of material failure due to the possible existence of micro defects, it was shown that the ductile behaviour of the austenitic cladding provides significant load shielding effects for cracks in the ferritic base metal underneath the cladding, which might be utilized in the fracture assessment of clad components.

Acknowledgement

The present work has been supported by the German Federal Department of Economics and Technology (BMWi) under grant no. 150 1278. The financial support is gratefully acknowledged.

References

- [1] ASTM Standard E 1921-05: *Standard Test Method for Determination of the Reference Temperature, T_0 , for Ferritic Steels in the Transition Range*, ASTM International, West Conshohocken, PA 2005.
- [2] *ASME Boiler and Pressure Vessel Code, Sec. XI*, American Society of Mechanical Engineers, New York 1995.
- [3] *KTA 3201: Komponenten des Primärkreises von Leichtwasserreaktoren*, Kerntechnischer Ausschuss, Bonn 1997 (in German).
- [4] SIMULIA: *ABAQUS Analysis User's Manual, Version 6.7*, ABAQUS Inc., Providence, RI, 2007.
- [5] SYSTUS International: *SYSWELD 2006 User's Reference Manual*, ESI Group, Paris 2007.
- [6] Blauel, J.G., Hodulak, L., Nagel, G., Schmitt, W. and Siegele, D.: *Effect of cladding on the initiation behaviour of finite length cracks in an RPV under thermal shock*, Nucl. Eng. Des. **171** (1997) 179-188.
- [7] Gurson, A.L.: *Continuum theory of ductile rupture by void nucleation and growth.: Part I - Yield criteria and flow rules for porous ductile media*, J. Eng. Mat. Techn. **99** (1977) 2-15.
- [8] Hodulak, L., Blauel, J.G., Siegele, D. and Urich, B.: *Thermal shock experiments on cracked clad plates*, Nucl. Eng. Des. **188** (1999) 139-147.
- [9] Hodulak, L. and Siegele, D.: *Fracture behavior of subclad cracks*, Fracture Mechanics: 26th Volume (Reuter, W.G., Underwood, J.H. and Newman, J.C., eds.), ASTM STP 1256, American Society for Testing and Materials, Philadelphia 1995, 417-429.

- [10] Hohe, J., Brand, M., Siegele, D., Varfolomeev, I., Sguaizer, Y., Schüler, J., Urich, B., Fehrenbach, C., Haas, E., Oeser, S., Möser, M., Varfolomeeva, V., Luckow, S. and Hardenacke, V.: *Bewertung von Rissen in der Plattierung*, Report S35/2007, Fraunhofer Institut für Werkstoffmechanik, Freiburg 2008 (in German).
- [11] Hohe, J., Hebel, J., Friedmann, V. and Siegele, D.: *Probabilistic failure assessment of ferritic steels using the master curve approach including constraint effects*, Eng. Frac. Mech. **74** (2007) 1274-1292.
- [12] Marie, S. and Chapuliot, S.: *Improvement of the calculation of the stress intensity factors for underclad and through-clad defects in a reactor pressure vessel steel subjected to a pressurised thermal shock*, Int. J. Pres. Ves. Piping **85** (2008) 517-531.
- [13] Marie, S. and Nédélec, M.: *A new plastic correction for the stress intensity factor of an under-clad defect in a PWR vessel subjected to a pressurized thermal shock*, Int. J. Pres. Ves. Piping **84** (2007) 159-170.
- [14] Siegele, D. and Brand, M.: *Numerical simulation of residual stresses due to the cladding process*, ASME-paper PVP 2007-26586, Proc. 2007 ASME Pressure Vessels and Piping Conf. (San Antonio, TX, July 22-26, 2007), CD-ROM.

List of Figures

1	Metallographic investigation, section oriented normal to the welding direction.	12
2	Yield curves for the different material zones and temperatures.	12
3	Specimens and set-up for large-scale fracture mechanics experiments.	13
4	Results of large-scale experiments: measured temperature distributions and load-deflection diagram.	13
5	Fractographic investigation.	14
6	Sequence of analyses in the multi-step simulation procedure.	14
7	Residual stresses in the crack plane before and after post weld heat treatment.	15
8	Finite element models for simulation of the large-scale experiments.	15
9	Fracture mechanics assessment of the large-scale experiments.	16

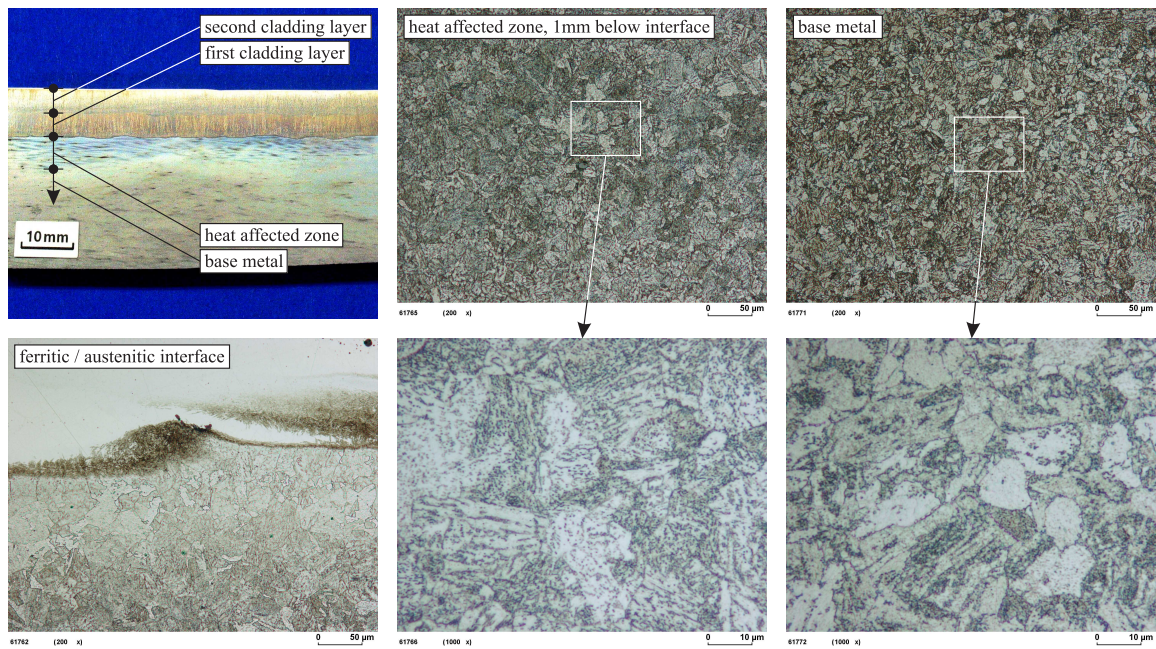


Figure 1: Metallographic investigation, section oriented normal to the welding direction.

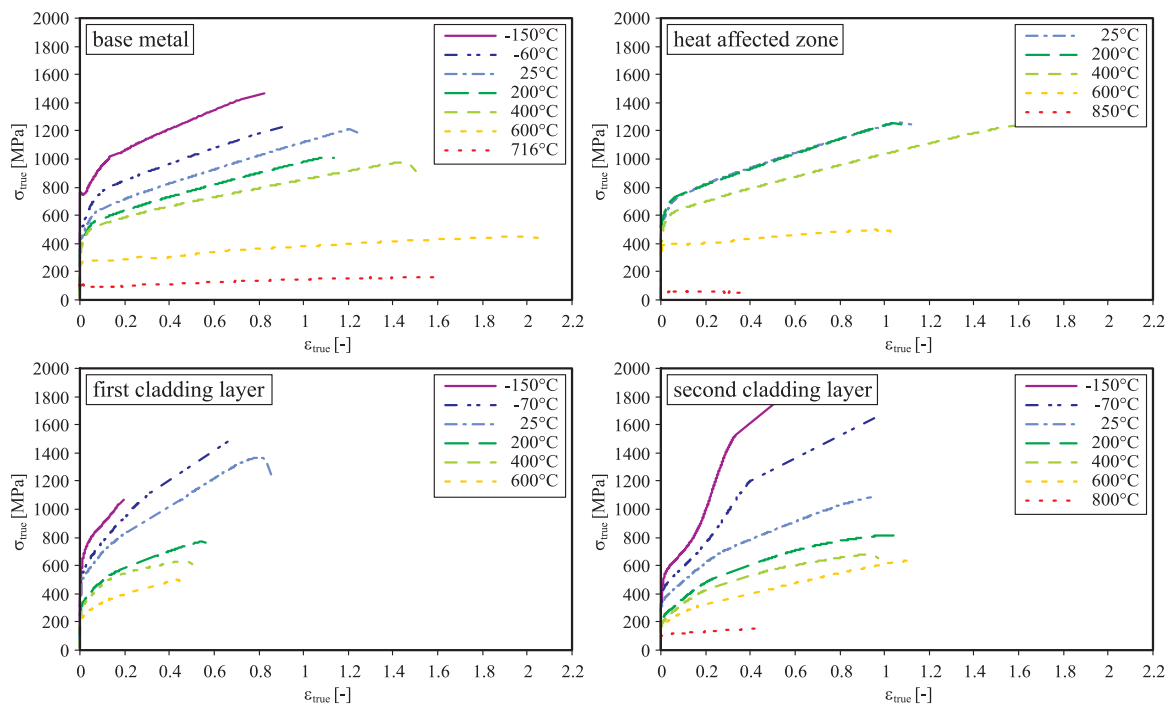


Figure 2: Yield curves for the different material zones and temperatures.

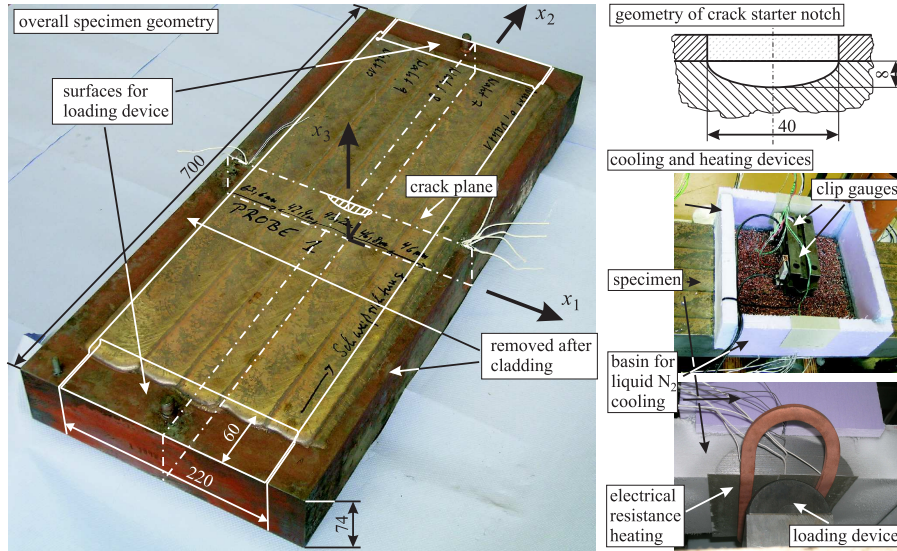


Figure 3: Specimens and set-up for large-scale fracture mechanics experiments.

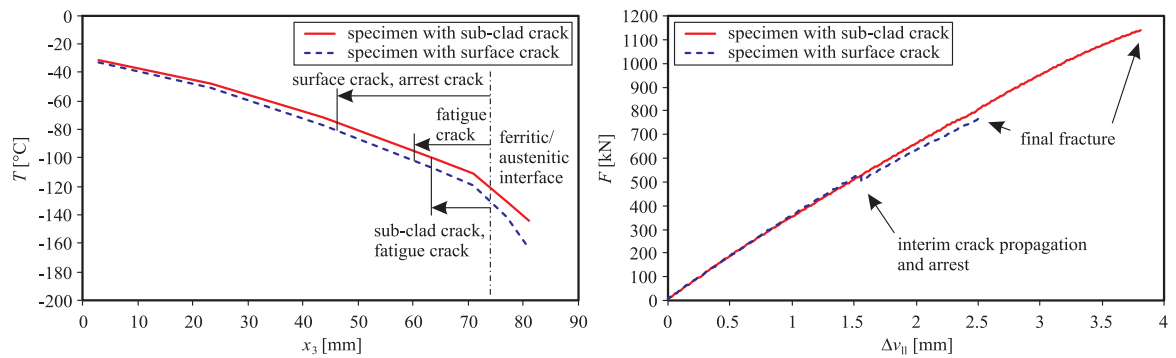


Figure 4: Results of large-scale experiments: measured temperature distributions and load-deflection diagram.

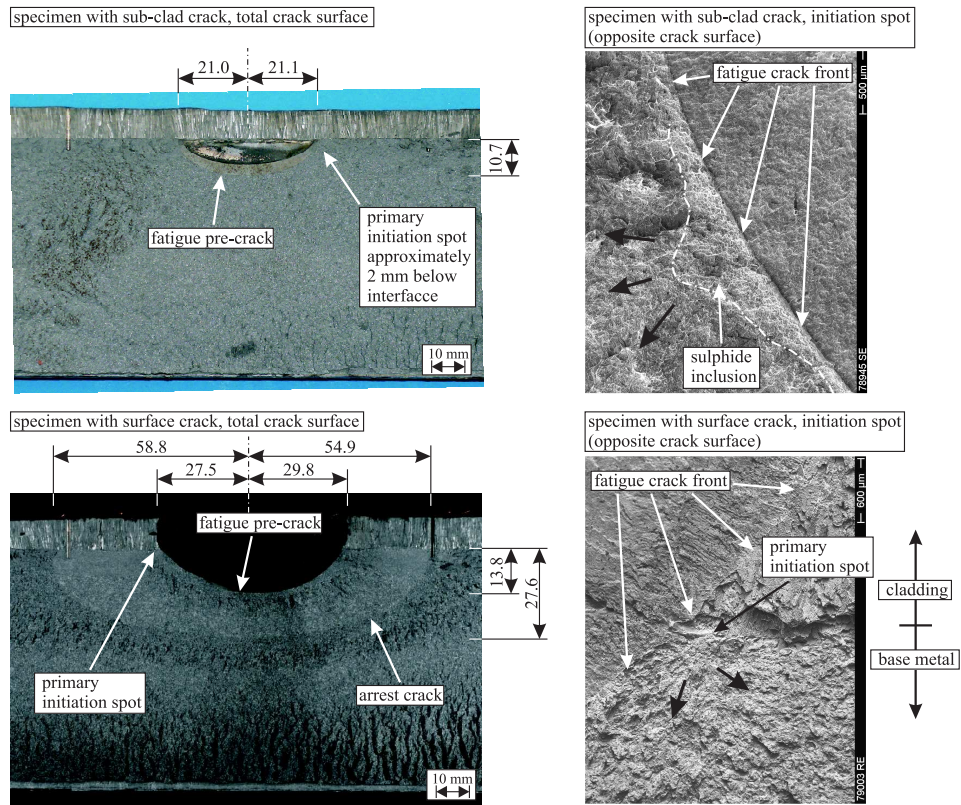


Figure 5: Fractographic investigation.

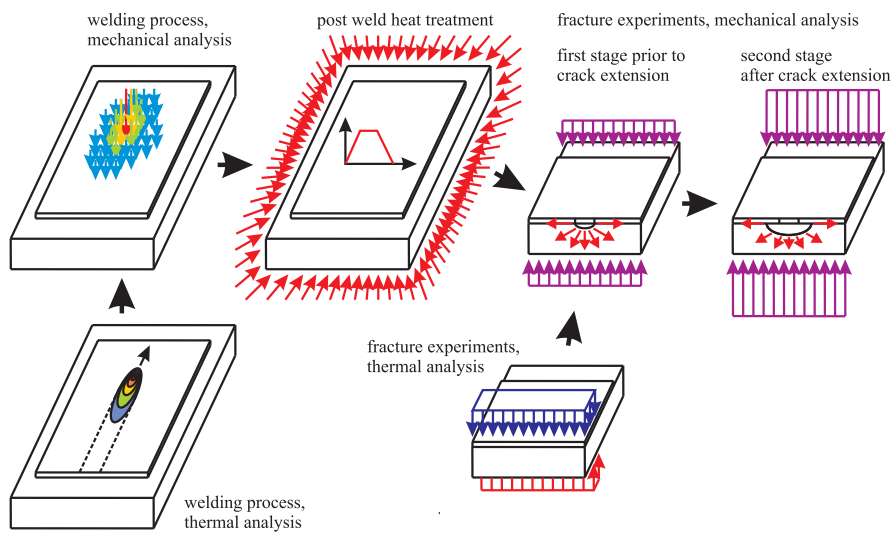


Figure 6: Sequence of analyses in the multi-step simulation procedure.

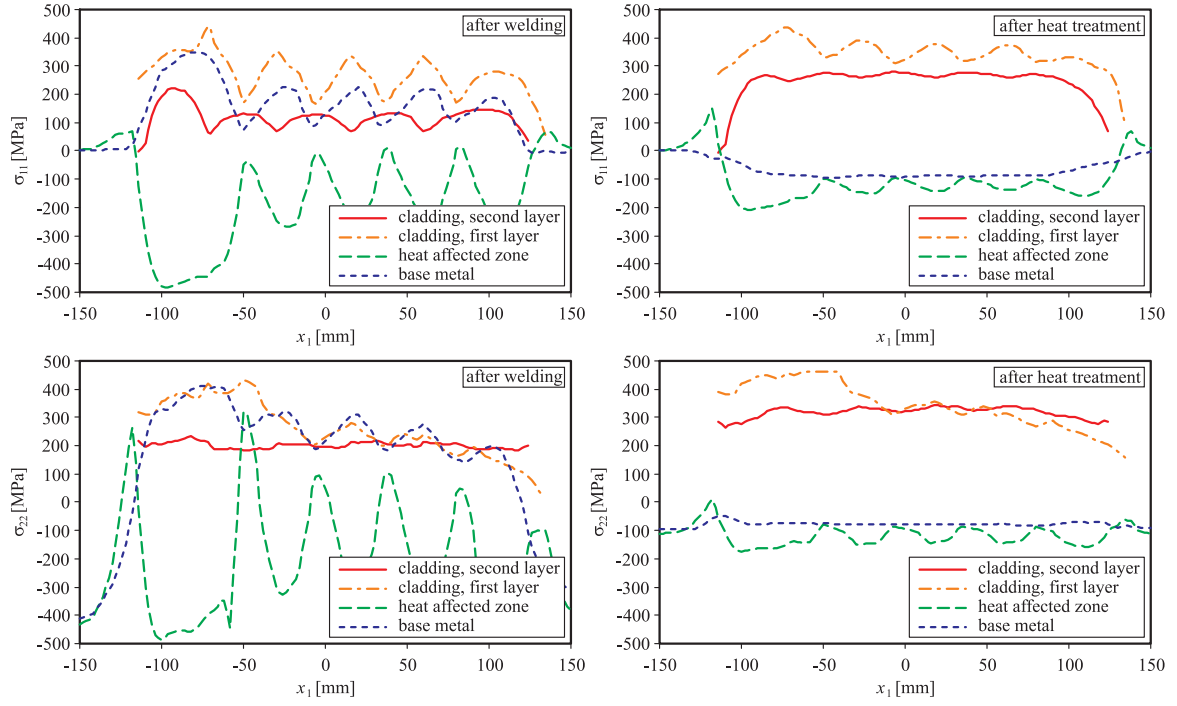


Figure 7: Residual stresses in the crack plane before and after post weld heat treatment.

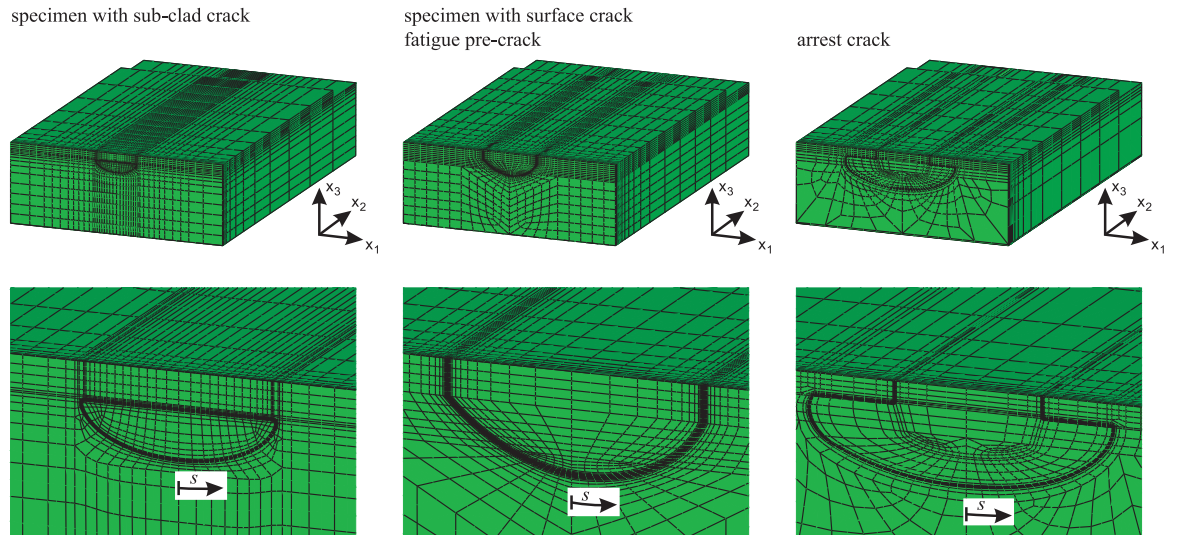


Figure 8: Finite element models for simulation of the large-scale experiments.

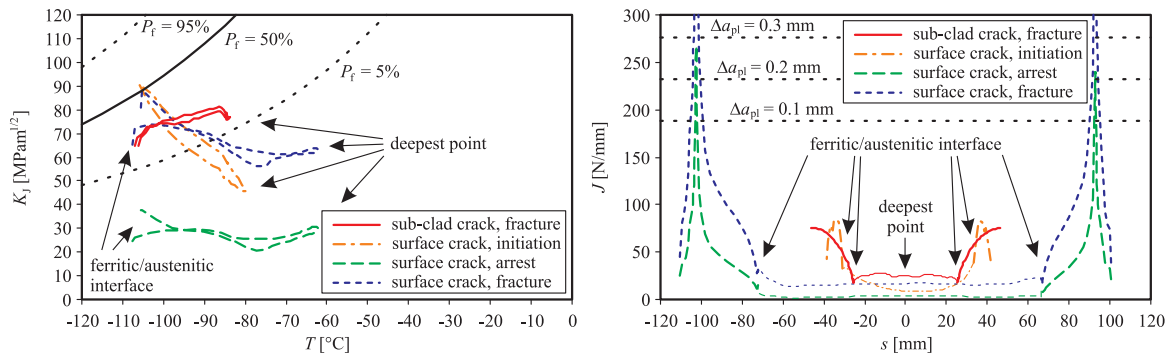


Figure 9: Fracture mechanics assessment of the large-scale experiments.